# Applications of the Miller equilibrium to extend tokamak computational models

W. M. Stacey
*Fusion Research Center and Nuclear and Radiological Engineering, Georgia Institute of Technology, 900 Atlantic Drive, Atlanta, Georgia 30332, USA*

(Received 9 October 2008; accepted 7 November 2008; published online 11 December 2008)

An analytical model for the equilibrium flux surface geometry, widely known as the Miller equilibrium model, has been exploited to improve a variety of simplified tokamak computation models that incorporate an approximate flux surface geometry. Also discussed are improved models for an effective unelongated toroidal plasma representation of elongated flux surfaces; mapping temperature (and density) gradients measured at one poloidal location to other poloidal locations and to an average gradient over the flux surface; interpreting experimental heat diffusivities from local temperature gradients and average conductive heat fluxes; calculating the poloidal distribution of radial conductive heat fluxes; and evaluating the gyroviscous angular momentum transport rate. © *2008 American Institute of Physics*. [DOI: 10.1063/1.3039946]

## I. INTRODUCTION

The "natural" coordinates for tokamak plasma physics computations are the nested magnetic flux surfaces because of the striking differences in particle and energy flows within and across these flux surfaces. However, there are many calculation models in tokamak plasma physics that utilize simpler, more conventional geometries. Such models generally employ, explicitly or implicitly, some approximation to the flux surfaces to enable exploitation of the great differences in flows across and within the flux surfaces to reduce the required dimensionality of the calculation.

Several years ago, Miller *et al.*[1] introduced an analytical equilibrium model for localized stability studies in which the flux surface is completely described by the aspect ratio, elongation, triangularity, and safety factor. We have recently been motivated (by an application[2] of the Miller equilibrium to estimate the poloidal heat flux distribution) to apply this Miller equilibrium model to improve one-dimensional calculation models that reflect two-dimensional effects on plasma transport by the incorporation of a simple analytical model for the plasma flux surface geometry. The purpose of this paper is to describe a number of such applications of the Miller equilibrium model.

## II. MILLER EQUILIBRIUM

### A. Geometry

Miller *et al.*[1] derived analytical expressions for an equilibrium flux surface in a plasma as shown in Fig. 1 with elongation $\kappa$, triangularity $\delta$, and displaced centers $R_0(r)$, where $r$ is the half-diameter of the plasma along the midplane with center located at distance $R_0(r)$ from the toroidal centerline.

The $R$ and $Z$ coordinates of this plasma are described by[1]

$$R(r) = R_0(r) + r\cos[\theta + x\sin\theta] \equiv R_0(r) + r\cos\xi,$$
$$Z(r) = \kappa r\sin\theta, \tag{1}$$

where $x \equiv \sin^{-1}\delta$.

The poloidal magnetic field in such flux surface geometry is[1]

$$RB_p = |\nabla\phi\times\nabla\psi| = \frac{\partial\psi}{\partial r}|\nabla r| = \frac{\frac{\partial\psi}{\partial r}\kappa^{-1}[\sin^2(\theta+x\sin\theta)(1+x\cos\theta)^2+\kappa^2\cos^2\theta]^{1/2}}{\cos(x\sin\theta)+\frac{\partial R_0}{\partial r}\cos\theta+[s_\kappa - s_\delta\cos\theta+(1+s_\kappa)x\cos\theta]\sin\theta\sin(\theta+x\sin\theta)}, \tag{2}$$

where $s_\kappa = r/\kappa\partial\kappa/\partial r$ and $s_\delta = r\partial\delta/\partial r/\sqrt{(1-\delta^2)}$ account for the change in elongation and triangularity, respectively, with radial location.

The shifted circle model (which leads to the Shafranov shift) yields[1]

$$\frac{\partial R_0}{\partial r} \equiv \Delta' = -\frac{r}{R_0}\left(\beta_p + \frac{1}{2}\ell_i\right) \tag{3a}$$

and a shifted ellipse model by Lao *et al.*[3] yields

 

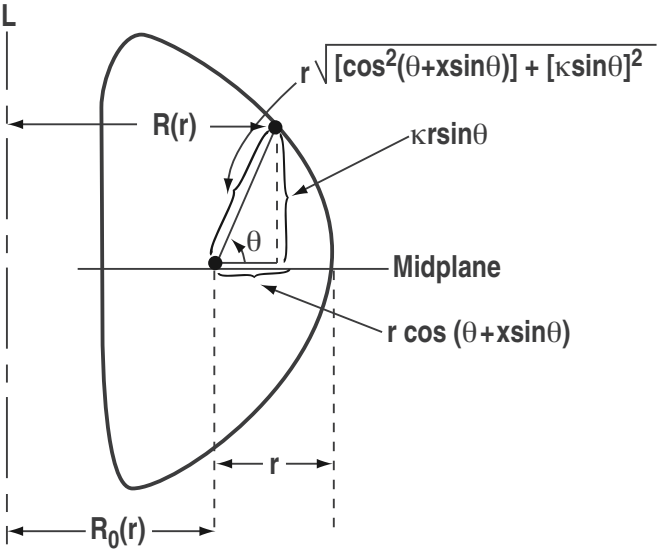


FIG. 1. Miller equilibrium parameters.

$$\frac{\partial R_0}{\partial r} = -\frac{r}{R_0}\left[\frac{2(\kappa^2+1)}{(3\kappa^2+1)}\left(\beta_p + \frac{1}{2}\ell_i\right) + \frac{1}{2}\frac{(\kappa^2-1)}{(3\kappa^2+1)}\right]. \tag{3b}$$

Here $\beta_p = nT/B_\theta^2/2\mu_0$ and $\ell_i$ is the internal inductance.

### B. Flux surface average

The flux surface average (FSA) of a quantity $A(r,\theta)$ in this flux surface geometry is

$$\langle A(r,\theta)\rangle \equiv \frac{\oint \frac{A(r,\theta)d\ell_p}{B_p}}{\oint \frac{d\ell_p}{B_p}} = \frac{\oint A(r,\theta)z(r,\theta)d\ell_p}{\oint z(r,\theta)d\ell_p}, \tag{4}$$

where

$$z(r,\theta) \equiv \frac{\cos(x\sin\theta) + \frac{\partial R_0}{\partial r}\cos\theta + [s_\kappa - s_\delta\cos\theta + (1+s_\kappa)x\cos\theta]\sin\theta\sin(\theta + x\sin\theta)}{[\sin^2(\theta+x\sin\theta)(1+x\cos\theta)^2 + \kappa^2\cos^2\theta]^{1/2}/\{R_0(r) + r\cos[\theta + x\sin\theta]\}} \tag{5}$$

and the differential poloidal length is (see Fig. 1)

$$d\ell_p = r\sqrt{[\cos^2(\theta + x\sin\theta) + \kappa^2\sin^2\theta]}d\theta. \tag{6}$$

## III. EQUIVALENT TOROIDAL MODELS

Complicated flux surface geometries are frequently reduced to effective one-dimensional toroidal models for transport calculations and experimental data interpretation. The more sophisticated of such models (the so-called "1.5D" models; e.g., Ref. 4) make use of a 2D MHD (magnetohydrodynamic) calculation of the flux surface geometry to construct an effective toroidal model that conserves certain properties of the equilibrium. Simpler models that use analytical representations of the flux surface geometry, instead of a 2D MHD calculation, are also commonly used (e.g., Ref. 5).

A common representation is the "elliptical equilibrium model" of an elongated plasma described by $R = R_0 + r\cos\theta, Z = \kappa r\sin\theta, B_p = B_{p0}/(1 + r/R_0\cos\theta)$. With reference to Fig. 2, an effective nonelongated toroidal model that preserves the area of the exterior flux surface of the elliptical equilibrium model with the same elongation, $\kappa$, as the actual flux surface is constructed by defining an effective radius variable $\bar{r}$ that is related to the actual radial variable in the horizontal midplane $r$ and the elongation by $\bar{r} = r\sqrt{1/2(1+\kappa^2)}$. This model preserves surface area but does not account for compression/expansion of the spacing between flux surfaces.

The Miller equilibrium model can be used to obtain an improved nonelongated toroidal model that takes into account triangularity and the "Shafranov shift" compression/expansion of flux surfaces, as well as the elongation. The area of the flux surface $\psi$ passing through the midplane radius $r$ in the Miller equilibrium model is

$$\begin{aligned} A(\psi) &= \oint_\psi d\ell_p \int_0^{2\pi} h_\phi d\phi = 2\pi \oint_\psi R d\ell_p \\ &= 2\pi r R_0(r)\int_0^{2\pi}\left[1 + \frac{r}{R_0(r)}\cos(\theta + x\sin\theta)\right] \\ &\quad \times[\cos^2(\theta + x\sin\theta) + \kappa^2\sin^2\theta]^{1/2}d\theta. \end{aligned} \tag{7}$$

The area of an unelongated torus with radial variable $\bar{r}$ is $A_c(\bar{r}) = 2\pi R_0(a)2\pi\bar{r}$. Equating the two areas and solving for

$$\begin{aligned} \bar{r} &= r\frac{R_0(r)}{2\pi R_0(a)}\int_0^{2\pi}\left[1 + \frac{r}{R_0(r)}\cos(\theta + x\sin\theta)\right] \\ &\quad \times[\cos^2(\theta + x\sin\theta) + \kappa^2\sin^2\theta]^{1/2}d\theta \end{aligned} \tag{8}$$

defines the radial variable of an equivalent toroidal model that preserves the surface area of the Miller equilibrium flux surface. The effective radius at the exterior surface of the torus is $\bar{a}$, determined by evaluating Eq. (8) for $r = a$, the half-radius at the horizontal midplane of the actual exterior flux surface.

A comparison calculation was made for a plasma representative of a DIII-D (Ref. 6) discharge with minor horizon-

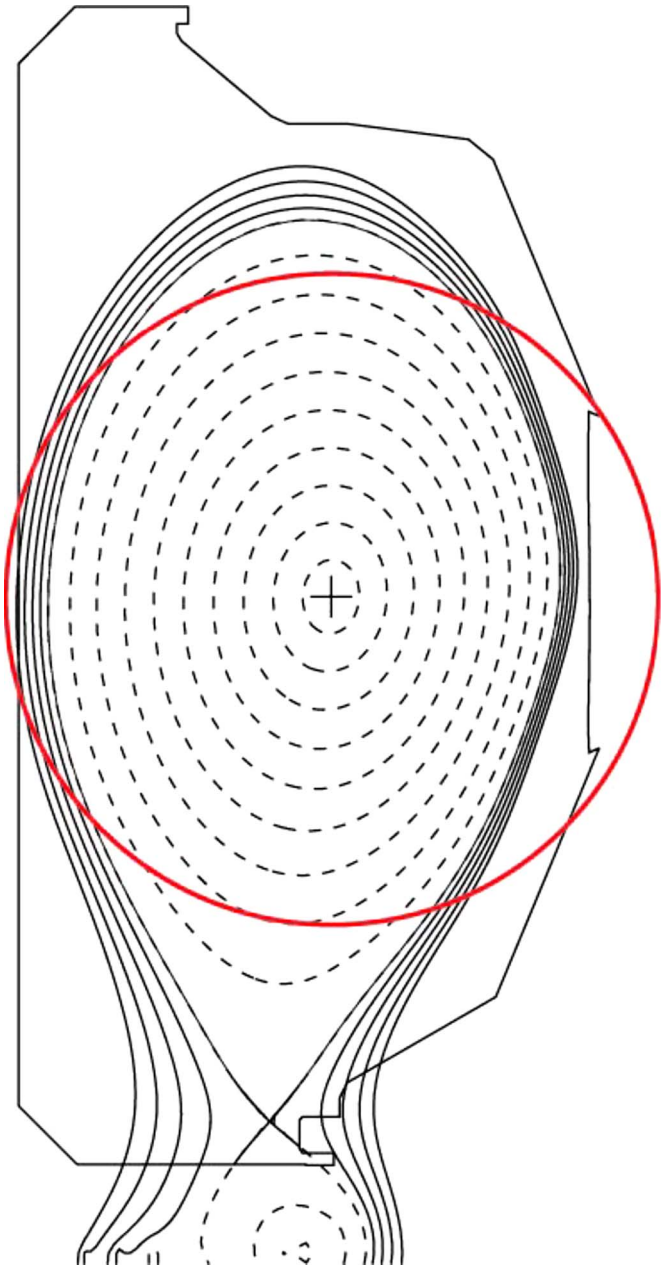

FIG. 2. (Color online) Effective toroidal model superimposed on flux surface geometry.

tal radius $a=0.583$ m, varying triangularity, elongation $\kappa=1.75$, and major radius $R_0(a)=1.77$ m. The elliptical model predicts for these parameters an effective circular plasma radius $\bar{a}=0.830$ m. Evaluation of Eq. (8) with $x=\sin^{-1}\delta$ yields almost the same value of $\bar{a}=0.817$ m for $\delta=0$, as shown in Table I. For nonzero values of the triangularity, the Miller model predicts increasingly smaller equivalent toroidal radii than the elliptical model to preserve surface area.

TABLE I. Effect of triangularity on effective toroidal radius and $H(a,\theta=0)$.

| $\delta$ Triangularity | $\bar{a}(m)$ Miller equil. | $\bar{a}(m)$ Elliptic equil. | $H(a,\theta=0)$ Miller equil. | $H(a,\theta=0)$ Elliptic equil. |
|---|---|---|---|---|
| 0.0 | 0.817 | 0.830 | 1.73 | 1.43 |
| 0.1 | 0.800 | ⋯ | 1.73 | ⋯ |
| 0.2 | 0.784 | ⋯ | 1.73 | ⋯ |
| 0.3 | 0.769 | ⋯ | 1.73 | ⋯ |
| 0.4 | 0.753 | ⋯ | 1.72 | ⋯ |
| 0.5 | 0.739 | ⋯ | 1.71 | ⋯ |
| 0.6 | 0.725 | ⋯ | 1.69 | ⋯ |
| 0.7 | 0.710 | ⋯ | 1.66 | ⋯ |
| 0.8 | 0.696 | ⋯ | 1.62 | ⋯ |
| 0.9 | 0.680 | ⋯ | 1.55 | ⋯ |

## IV. INTERPRETATION OF THERMAL CONDUCTIVITIES FROM MEASURED TEMPERATURE GRADIENTS

Another application of the Miller equilibrium that immediately comes to mind is in the inference of experimental thermal diffusivities from measured temperature gradients in tokamaks. The measured temperature gradient $(dT/dr)_{\rm exp}$ pertains of course to the location $(r,\theta_{\rm exp})$ at which the measurement is made [although sometimes the reported value is mapped along flux surfaces to another location such as the outboard midplane at $(r,\theta=0)$]. On the other hand, one-dimensional radial transport codes of the type discussed in the previous section calculate an average conductive heat flux $\langle q(r)\rangle$. In order to use the calculated average heat flux and the local (in $\theta$) measured temperature gradient in the heat conduction relation to infer a measured thermal diffusivity $\chi=-q/n(dT/dr)\equiv qL_T/nT$, the local temperature gradient scale length must be mapped into an average value over the flux surface

$$\begin{aligned}(L_T)_{\rm exp} &\equiv -T(dr/dT)_{\rm exp}\Rightarrow\langle L_T\rangle\\ &= -T(dr/dT)_{\rm exp}[\langle dr\rangle/dr(\theta_{\rm exp})]\\ &\equiv (L_T)_{\rm exp}[\langle dr\rangle/dr(\theta_{\rm exp})]\\ &= (L_T)_{\rm exp}[|\nabla r(\theta_{\rm exp})|/\langle|\nabla r|\rangle].\end{aligned} \tag{9}$$

From Eq. (2), the local $|\nabla r|$ may be written

$$|\nabla r(r,\theta)| = \frac{\kappa^{-1}[\sin^2(\theta+x\sin\theta)(1+x\cos\theta)^2+\kappa^2\cos^2\theta]^{1/2}}{\cos(x\sin\theta)+\dfrac{\partial R_0}{\partial r}\cos\theta+[s_\kappa-s_\delta\cos\theta+(1+s_\kappa)x\cos\theta]\sin\theta\sin(\theta+x\sin\theta)}. \tag{10}$$

Using this in Eq. (4) yields an expression for the FSA value

$$\langle|\nabla r(r)|\rangle = \frac{\int_0^{2\pi}[R_0(r)+r\cos(\theta+x\sin\theta)][\cos^2(\theta+x\sin\theta)+\kappa^2\sin^2\theta]^{1/2}d\theta}{\int_0^{2\pi}F(r,\theta)[R_0(r)+r\cos(\theta+x\sin\theta)][\cos^2(\theta+x\sin\theta)+\kappa^2\sin^2\theta]^{1/2}d\theta}, \tag{11}$$

where

$$F(r,\theta) = \frac{\cos(x\sin\theta)+\dfrac{\partial R_0}{\partial r}\cos\theta+[s_\kappa - s_\delta\cos\theta+(1+s_\kappa)x\cos\theta]\sin\theta\sin(\theta+x\sin\theta)}{\kappa^{-1}[\sin^2(\theta+x\sin\theta)(1+x\cos\theta)^2+\kappa^2\cos^2\theta]^{1/2}}. \tag{12}$$

The FSA value of the temperature gradient scale length, $\langle L_T\rangle = -\langle T/(dT/dr)\rangle$, which is the quantity needed for the inference of experimental thermal diffusivity using the average heat flux calculated by 1D transport codes, is related to the local value of the temperature gradient scale length, $L_T(\theta) = -T/(dT/dr)_\theta$, which is the quantity measured, by

$$\frac{\langle L_T(r)\rangle}{L_T(r,\theta)} = \frac{|\nabla r(r,\theta)|}{\langle|\nabla r(r)|\rangle} \equiv H(r,\theta). \tag{13}$$

For the case $\theta=0$, corresponding to the outboard midplane location of the measured gradient scale lengths, Eq. (10) reduces to the Shafranov shift correction

$$|\nabla(r,\theta=0)| = \frac{1}{(1+\partial R_0/\partial r)}. \tag{14}$$

A series of calculations was performed for the same plasma model with minor horizontal radius $a=0.583$ m, varying triangularity, elongation $\kappa=1.75$, and major radius $R_0(a)=1.77$ m, using Eqs. (10)–(13) with $s_\kappa=0, s_\delta=0$ and using the elliptical model discussed in the previous section, for which $H(r,\theta=0)=\sqrt{1/2(1+\kappa^2)}=1.43$. The results are shown in Table I. The Miller model predicts values of $H(a,\theta=0)$ that are 10%–20% larger than those predicted by the elliptical model.

Following the procedures described in Ref. 5, the thermal diffusivities were calculated from measured temperature gradients (mapped to the outboard midplane) for a different ELMing H-mode DIII-D discharge between edge-localized modes (ELMs). This discharge had parameters ($I=1.0$ MA, $B=1.6$ T, $\kappa=1.83$, $\delta=0.44$, $\Delta'=-0.25$). Both the effective radius of the unelongated toroidal model and the factor $H$ given by Eq. (13) were calculated first with the elliptical equilibrium model and then with the Miller equilibrium model, as discussed above. Use of the Miller model instead of the simpler elliptical model to represent the flux surface geometry increases the inferred thermal diffusivities significantly, as shown in Fig. 3.

Neglecting the effect of the radial variation of the elongation and triangularity ($s_\kappa=0, s_\delta=0$) and also momentarily neglecting the triangularity ($\delta=0$), reduces Eq. (13) to a form that more readily exhibits the various factors involved

$$\frac{\langle L_T(r)\rangle}{L_T(r,\theta=0)} = H(r,\theta=0) = \frac{\displaystyle\int_0^{2\pi}\frac{\kappa\left[1+\dfrac{\partial R_0}{\partial r}\cos\theta\right]}{[1+(\kappa^2-1)\cos^2\theta]^{1/2}}[R_0+r\cos\theta][1+(\kappa^2-1)\sin^2\theta]^{1/2}d\theta}{\left[1+\dfrac{\partial R_0}{\partial r}\right]\displaystyle\int_0^{2\pi}[R_0+r\cos\theta][1+(\kappa^2-1)\sin^2\theta]^{1/2}d\theta}. \tag{15}$$

## V. PREDICTION OF POLOIDAL DISTRIBUTION OF CONDUCTIVE HEAT FLUX

One-dimensional transport codes calculate an average conductive heat flux, $\langle q\rangle$. Assuming that the density, temperature and thermal diffusivity are uniform over the flux surface, the poloidal dependence of the conductive heat flux must arise through the poloidal dependence of the radial temperature gradient

$$\begin{aligned} q(r,\theta) &= n(r)T(r)\chi(r)L_T^{-1}(r,\theta) \\ &= n(r)T(r)\chi(r)\langle L_T(r)\rangle^{-1}H(r,\theta). \end{aligned} \tag{16}$$

The value of $H(r,\theta)\equiv q(r,\theta)/\langle q(r)\rangle \equiv \langle L_T(r)\rangle/L_T(r,\theta)$ calculated from Eqs. (10)–(13) near the separatrix ($r\to a$) of one of the DIII-D plasmas previously described ($\Delta'=-0.25, \kappa=1.75, r/R=1/3$) is plotted in Fig. 4. The curve labeled "symmetric" uses averaged values $\kappa=1.77$, $\delta=0.07$ for all values of $\theta$, while the curve labeled "asym-

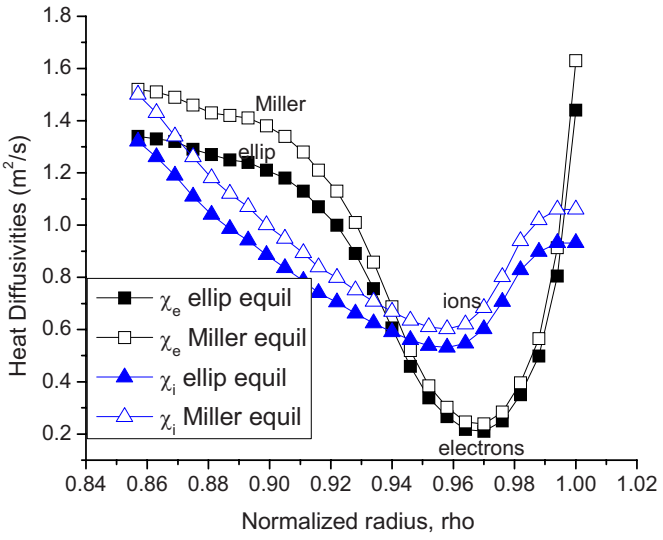


FIG. 3. (Color online) Inferred experimental thermal diffusivities for a DIII-D shot using the elliptical and the Miller models to represent the flux surface geometry.

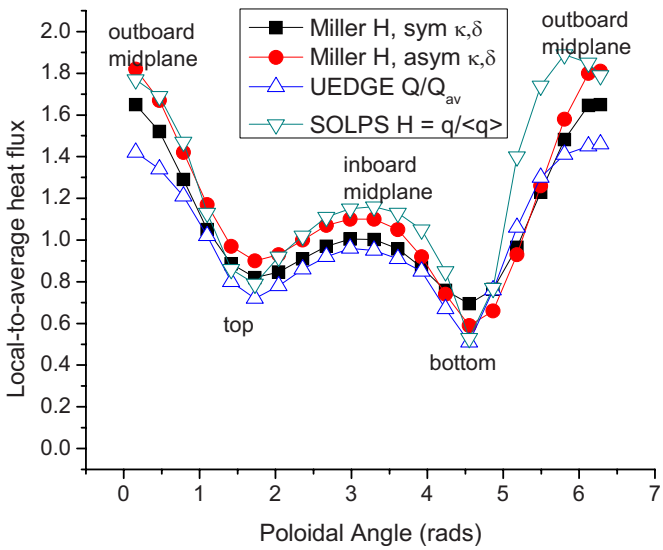


FIG. 4. (Color online) Predicted poloidal distribution of the conductive heat flux near the separatrix for a DIII-D shot.

metric" uses experimental values $\kappa_{top}=1.50, \delta_{top}=0.0$ in the upper half $0\leqslant\theta\leqslant\pi$ and $\kappa=2.32, \delta=0.14$ in the lower half $\pi\leqslant\theta\leqslant 2\pi$.

For comparison, the heat flux through a flux surface about 6 cm inside the separatrix calculated[7,8] by the 2D transport codes UEDGE (Ref. 9) and SOLPS (Ref. 10) using the same temperature and density data are also shown. The UEDGE heat flux includes the convective component as well as the conductive component and is normalized to the average value over the flux surface (rather than the flux surface average normalization of H). The SOLPS result is the conductive heat flux normalized to its FSA, which is identical to the quantity H as calculated by SOLPS. The bunching of the flux surfaces at the outboard midplane and the elongation at the top and bottom of the plasma account for the distribution. The Miller model does not contain an explicit representation of the lower divertor present in this shot, and the difference between the Miller model prediction and the numerical results increased as the separatrix was approached.

## VI. MAPPING RADIAL GRADIENTS TO DIFFERENT POLOIDAL LOCATIONS

The above formalism can also be used to map a radial gradient (temperature or density or any other quantity) determined (by measurement or calculation) at a poloidal location $\theta_1$ to a different location $\theta_2$. The gradient scale length of any flux surface quantity $X, L\equiv -X/(dX/dr)$ maps according to Eq. (13),

$$L(r,\theta_2)=H^{-1}(r,\theta_2)\langle L(r)\rangle=\frac{H(r,\theta_1)}{H(r,\theta_2)}L(r,\theta_1). \tag{17}$$

## VII. GYROVISCOUS TORQUE

The neoclassical gyroviscous torque can be written[11]

$$\begin{aligned}\langle R^2\nabla\phi\cdot\nabla\cdot\Pi\rangle_{gv}&=\frac{1}{V'}\frac{\partial}{\partial\psi}(V'\langle R^2\nabla\phi\cdot\Pi\cdot\nabla\psi\rangle)\\&=\frac{1}{V'}\frac{\partial}{\partial\psi}(V'\langle R\mathbf{n}_\phi\cdot\Pi\cdot\mathbf{n}_\psi RB_p\rangle)\\&=\frac{1}{V'}\frac{\partial}{\partial\psi}(V'\langle R^2B_p\Pi_{\phi\psi}\rangle),\end{aligned} \tag{18}$$

where

$$\Pi_{\phi\psi}=-\frac{nmT}{ZeB}R\frac{\partial(V_\phi/R)}{\partial\ell_p},\quad V'=\oint\frac{d\ell_p}{B_p}. \tag{19}$$

When the elliptical equilibrium model $R=R_0+r\cos\theta$, $Z=\kappa r\sin\theta$, $B_p(r,\theta)=B_p(r)/(1+r\cos\theta/R_0)$ is used, this becomes[11,12]

$$\langle R^2\nabla\phi\cdot\nabla\cdot\Pi_j\rangle_{gv}\equiv Rn_jm_j\nu_{dj}V_{\phi j}\cong\frac{1}{2}\Theta_jG_j\frac{n_jm_jT_j}{Z_jeB}V_{\phi j}, \tag{20}$$

where an effective angular momentum transfer frequency

$$\nu_d=\frac{T_j}{2R_0^2e_jB^o}G_j\Theta_j \tag{21}$$

has been defined. The poloidal asymmetry and spatial gradient factors are

$$\begin{aligned}\Theta_j&=(4+\tilde{n}_j^c)\tilde{V}_{\phi j}^s+\tilde{n}_j^s(1-\tilde{V}_{\phi j}^c),\\G_j(r)&=r(L_{n_j}^{-1}+L_{T_j}^{-1}+L_{V_{\phi j}}^{-1})\end{aligned} \tag{22}$$

and the poloidal asymmetries have been normalized $\tilde{n}_j^{c,s}=n_j^{c,s}/(r/R_0)$, $\tilde{V}_j^{c,s}=V_j^{c,s}/(r/R_0)$.

Low-order Fourier expansions

$$n_j(r,\theta) \cong n_j^0(r)(1 + n_j^s \sin\theta + n_j^c \cos\theta),$$
$$V_{\phi j}(r,\theta) \cong V_{\phi j}^0(r)(1 + V_{\phi j}^s \sin\theta + V_{\phi j}^c \cos\theta) \tag{23}$$

have been used in deriving Eqs. (20) and (21). These Fourier components of the density and rotation velocities can be calculated by taking low order Fourier moments of the momentum and particle balance equations to relate the poloidal asymmetry components to the density asymmetry components

$$V_\theta^0 V_\theta^c = -r\frac{n_e^0}{n^0}\nu_{\text{ion}}(n_e^s) - V_\theta^0(\varepsilon + n^c),$$
$$V_\theta^0 V_\theta^s = r\frac{n_e^0}{n^0}\nu_{\text{ion}}(\varepsilon + n_e^c) - V_\theta^0 n^s \tag{24}$$

and to calculate the density asymmetry components.[13,14]

The radial component of the momentum balance then can be used to relate the toroidal velocity coefficients to the poloidal density coefficients[14]

$$V_{\phi j}^0 V_{\phi j}^s = r\nu_{\text{ion}j}\frac{n_e^0 B_\phi^0}{n_j^0 B_\theta^0}(\varepsilon + n_e^c + n_{oj}^c) + \left[\frac{E_r}{B_\theta^0} - P_j'\right]n_j^s - V_{\phi j}^0 n_j^s \tag{25a}$$

and

$$V_{\phi j}^0 V_{\phi j}^c = -r\nu_{\text{ion}j}\frac{n_e^0 B_\phi^0}{n_j^0 B_\theta^0}(n_e^s + n_{oj}^s) + \left[\frac{E_r}{B_\theta^0} - P_j'\right](2\varepsilon + n^c) - V_{\phi j}^0(\varepsilon + n^c), \tag{25b}$$

where $P_j' = (1/n_j^0 e_j)B_\theta^0 \partial p_j^0/\partial r$ and the electron density asymmetries are related to the ion density asymmetries by charge neutrality

$$n_e^{c,s} = \frac{Z_j \bar{n}_j n_j^{c,s} + Z_k \bar{n}_k n_k^{c,s}}{Z_j \bar{n}_j + Z_k \bar{n}_k} \equiv \gamma_j \bar{n}_j + \gamma_k \bar{n}_k. \tag{26}$$

With the Miller equilibrium model described above, the same Eqs. (18) and (19) obtain, leading to the explicit relation

$$\langle R^2 \nabla\phi \cdot \nabla \cdot \Pi_j \rangle_{gv} = \frac{\frac{-\partial}{\partial\psi}\oint R^3 \frac{n_j m_j T_j}{Z_j e B}\frac{\partial(V_{\phi j}/R)}{\partial \ell_p} d\ell_p}{\oint \frac{d\ell_p}{B_p}} = \frac{\frac{-\partial}{\partial r}\oint R^3 \frac{n_j m_j T_j}{Z_j e B}\frac{\partial(V_{\phi j}/R)}{\partial \theta} d\theta}{\oint \frac{d\ell_p}{B_p}\frac{\partial\psi}{\partial r}}, \tag{27}$$

where

$$\frac{\partial\psi}{\partial r}\frac{d\ell_p}{B_p} = r\kappa\frac{F(\theta)R(\theta)[\cos^2(\theta + x\sin\theta) + \kappa^2\sin^2\theta]^{1/2}d\theta}{[\sin^2(\theta + x\sin\theta)(1 + x\cos\theta)^2 + \kappa^2\cos^2\theta]^{1/2}}. \tag{28}$$

Evaluation of these relations leads again to Eq. (21) for the effective angular momentum transport frequency, but now with the radial gradient factor

$$G_j = r\left(L_{n_j}^{-1} + L_{T_j}^{-1} + L_{V_{\phi j}}^{-1} - \frac{1}{R_0}\frac{dR_0}{dr}\right) \tag{29}$$

modified to take into account the "Shafranov shift" effect of the flux surface compression/expansion, and with the poloidal asymmetry factor now given by

$$\Theta_j = \frac{2(A+B)/\varepsilon^2}{\kappa C}, \tag{30}$$

where

$$A = \oint (1 + n^c\cos\theta + n^s\sin\theta)(1 + \varepsilon\cos\theta)(1 + \varepsilon\cos\xi)^2(V_\phi^s\cos\theta - V_\phi^c\sin\theta)d\theta,$$
$$B = \varepsilon\oint (1 + n^c\cos\theta + n^s\sin\theta)(1 + \varepsilon\cos\theta)(1 + \varepsilon\cos\xi)(1 + x\cos\theta)\sin\xi(1 + V_\phi^s\sin\theta + V_\phi^c\cos\theta)d\theta,$$
$$C = \oint \left\{\frac{[\cos^2\xi + \sin^2\theta]^{1/2}(1 + \cos\xi)\left\{\cos(x\sin\theta) + \frac{dR_0}{dr}\cos\theta + [s_\kappa - s_\delta\cos\theta + (1 + s_\kappa)x\cos\theta]\sin\theta\sin\xi\right\}}{[\sin^2\xi(1 + x\cos\theta)^2 + \kappa^2\cos^2\theta]}\right\}d\theta, \tag{31}$$
$$\xi \equiv \theta + x\sin\theta.$$

In the limit $\kappa \to 1, \delta \to 0$, Eqs. (30) and (31) reduce identically to the first of Eqs. (22).

The effects of using the Miller equilibrium model instead of the simpler elliptic equilibrium model to evaluate the gyroviscous torque are (i) to add a "Shafranov shift" effect in the radial gradient term $G_j$ and (ii) to introduce a new form for the poloidal asymmetry factor $\Theta_j$. Neither of these changes in factors should, in themselves, produce new

terms that would cause an order of magnitude or larger change in the predicted gyroviscous torque. However, use of the Miller equilibrium in the evaluation of the poloidal asymmetries themselves $(n^{s,c}, V^{s,c})$ might be expected to produce both significantly larger asymmetries and a gyroviscous torque of significantly larger magnitude. In order to investigate this, it will be necessary to extend the solution procedure[12–14] for the Fourier moments of the poloidal momentum balance equation to be based on the Miller equilibrium model, and that will be the subject of a future paper.

## VIII. SUMMARY

The Miller equilibrium model, an analytical representation of the flux surface geometry that includes elongation, triangularity, and "Shafranov shift" flux surface compression/expansion, has been applied to improve several practical computation models for tokamak plasmas that incorporate an analytical treatment of the flux surface geometry. Improved models for an effective unelongated toroidal plasma representation of elongated flux surfaces, for mapping temperature (and density) gradients measured at one poloidal location to other poloidal locations and to an average gradient over the flux surface, for interpreting experimental heat diffusivities from local experimental temperature gradients and calculated average conductive heat fluxes, for calculating the poloidal distribution of radial conductive heat fluxes, and for evaluating the gyroviscous angular momentum transport rate were discussed. Illustrative numerical calculations were presented for DIII-D plasmas.

## ACKNOWLEDGMENTS

The author is grateful to J. D. Callen for motivating him by example to work out the consequences of applying the Miller equilibrium to these sorts of models and for comments on an early version of the paper. He is also grateful to T. D. Rognlien and J. M. Canik for allowing him to use their calculations for the poloidal heat flux distributions with UEDGE and SOLPS, respectively, that are shown in Fig. 3. Finally, he is grateful to R. J. Groebner for providing Fig. 2.

[1] R. L. Miller, M. S. Chu, J. M. Greene, Y. R. Lin-Liu, and R. E. Waltz, Phys. Plasmas **5**, 973 (1998).
[2] J. D. Callen, University of Wisconsin (ret), personal communication (2008).
[3] L. L. Lao, S. P. Hirshman, and J. Wieland, Phys. Fluids **24**, 1431 (1981).
[4] H. St. John, *Proceedings of the 15th International Conference on Plasma Physics and Controlled Fusion, Seville, 1994* (IAEA, Vienna, 1995), Vol. 3, p. 603.
[5] W. M. Stacey and R. J. Groebner, Phys. Plasmas **13**, 072510 (2006).
[6] J. Luxon, Nucl. Fusion **42**, 614 (2002).
[7] T. D. Rognlien, Lawrence Livermore National Laboratory, personal communication (2008).
[8] J. M. Canik, Oak Ridge National Laboratory, personal communication (2008).
[9] T. D. Rognlien, D. D. Ryutov, N. Mattor, and G. D. Porter, Phys. Plasmas **6**, 1851 (1999); Contrib. Plasma Phys. **38**, 152 (1998); Plasma Phys. Controlled Fusion **47**, A283 (2005).
[10] V. A. Rozhansky, S. P. Voskoboynikov, E. G. Kaveeva, D. P. Coster, and R. Schneider, Nucl. Fusion **41**, 387 (2001); **42**, 1110 (2002); **43**, 614 (2003); Contrib. Plasma Phys. **46**, 575 (2006).
[11] W. M. Stacey and D. J. Sigmar, Phys. Fluids **28**, 2800 (1985).
[12] W. M. Stacey, R. W. Johnson, and J. Mandrekas, Phys. Plasmas **13**, 062508 (2006).
[13] W. M. Stacey, Contrib. Plasma Phys. **46**, 122 (2006).
[14] W. M. Stacey, Phys. Plasmas **15**, 012501 (2008).